Dynamic Constitutive Model and Impact Resistance of Q460 Steel

Xiuhua Zhang, Shuang Yuan

Abstract—**High-strength steel has increasingly been utilized in major public structures and infrastructure both in the country and around the world, showcasing its wide-ranging potential for application. However, current research on Q460 steel under dynamic loading is limited. In this study, the dynamic mechanical behavior of Q460 material is investigated under various strain rates ranging from 4×10^{-4} to 1083 s^{-1}. Using a split Hopkinson pressure bar, quasistatic tensile and dynamic tests were conducted. The findings demonstrated that Q460 significantly affected the sensitivity to the strain rate. To establish a rate-dependent constitutive model for this material, Johnson-Cook (J-C) model was used to fit the stress-strain curves. The dynamic increase factor was calculated based on experimental data and predicted using the Cowper-Symonds (C-S) model. A numerical simulation was performed using ANSYS to evaluate the precision of the parameters used in the models, and the results revealed that the J-C model can effectively predict the stress-strain curves. Finite element analysis of the dynamic response of Q460 steel under blast loading was also performed based on the fluid-structure interactions. The test findings can serve as foundational data for future studies, and the constitutive model can be utilized for analyzing the dynamic performance of Q460 components.**

Index Terms—**Q460 high-strength steel, SHPB, constitutive model, numerical analysis, fluid-structure interaction**

I. Introduction

THE extensive use of steel structures has resulted in the application of high-strength steel to large-span, high-load-bearing, and lightweight structures, owing to its light weight, high strength, excellent seismic performance, and low energy consumption [1]-[3]. Moreover, the application of high-strength steel is consistent with the trend of green development [4]. According to GB 50017-2017[5], the grade of the steel was extended to Q460 (460 MPa). Research and scholarly attention has been notably drawn to steels boasting a yield strength of 460 MPa. Fincato et al. [6] evaluated the failure behavior of Q460 steel under monotonic loading using a coupled elastoplastic damage constitutive model. Wang et al. [7] conducted experimental and numerical simulation studies on the creep buckling of Q460 steel columns under high-temperature conditions and investigated the effects of the aspect ratio, load ratio, temperature, and geometric defects on creep buckling. Liao et al. [8] conducted quasi-static tests on welded cruciform beam-column joints of Q460 high-strength steel and examined their seismic performance by comparing the results with those of finite element analysis. Recently, Zhao et al. [9] conducted experimental research and numerical simulations on welded I-shaped continuous beams of Q460 high-strength steel. Compared with the current regulations, they proposed recommendations that are more suitable for the overall buckling capacity of Q460 single-symmetric I-shaped continuous beams made of high-strength steel. Yang et al. [10] systematically investigated the dynamic constitutive modeling of structural steels (Q235, Q355, Q460, and S960) and established a database of dynamic test results. Previous studies on Q460 steel included investigations of its material and static loading properties, which provided a theoretical basis for subsequent numerical simulations of this material under impact loading.

Explosive impact events pose a serious threat to safety. With the development of ultra-high-rise buildings, the local occurrence of explosions may lead to the collapse of an entire building [11]. Thus, beyond material dynamic properties, assessing component behavior under blast conditions is critical [12]. The split Hopkinson pressure bar (SHPB) experimental device has emerged as the most widely employed apparatus for assessing these properties, owing to its straightforward design and user-friendliness [13]-[15]. Dong [16] utilized ANSYS/ LS-DYNA to establish a three-dimensional model of a SHPB experimental device. The reliability of the finite element simulation was comprehensively examined by considering various aspects, such as appropriate element selection, effective hourglass control, optimal minimum time step, meticulous mesh division, accurate contact setting, and precise initial loading conditions. Ji [17] performed several investigations based on a material testing system of three different heat treatment states of 45# steel and true stress-true strain curves under different Hopkinson loading conditions. The parameters to be determined in the Johnson-Cook (J-C) constitutive relationship were fitted using the least-squares method, and the strain-rate hardening index was corrected. Zhang [18] conducted quasi-static and SHPB tests on Q235B and Q345B steels to obtain J-C and Cowper-Symonds (C-S) model parameters for Q235B and Q345B steels. Forni et al. [19] investigated the dynamic mechanical properties of S355 steel to establish a foundation for a continuous collapse analysis. Acharya [20] conducted SHPB experiments to examine the compressive behavior of an Al 6061-T6 alloy under various strain rates. Chen et al. [21]-[22] conducted a sequence of investigations on the mechanical properties of Q345 and

Manuscript received October 24, 2024; revised May 2, 2025.

Xiuhua Zhang is a professor and doctoral supervisor of Civil Engineering and Transportation of Northeast Forestry University, Harbin, China. (corresponding author to provide e-mail: zhangxh2000@163.com).

Shuang Yuan is a Graduate student of Civil Engineering and Transportation of Northeast Forestry University, Harbin, China. (e-mail: m13136766231@163.com).

Q420 steels under intermediate strain rates by employing a high-speed tensile testing machine and developed a rate-dependent model to enhance the accuracy of the dynamic response prediction. Yang et al. [23] conducted experimental research on the dynamic properties of Q550 steel at various strain rates and proposed J-C and C-S constitutive models that accurately predicted the dynamic behavior of a material under fast loading conditions. Yang et al. [24]-[25] investigated the strain rate effect of S690 steel, developed a dynamic constitutive model, and modified the J-C model to obtain an improved version applicable to S690 steel. Mei [26] examined the dynamic mechanical properties of stainless steel composite plates at high strain rates and established a constitutive model. Jing et al. [27] performed dynamic tensile tests on pre-fatigued specimens using an SHPB device across a wide range of strain rates. Considering the variable strain rate hardening coefficient and initial equivalent fatigue damage, this resulted in an enhanced J-C model describing the plasticity behavior of D1 railway wheels and U71MnG rail steels. Huang et al. [28] proposed a J-C constitutive model to accurately capture the plastic deformation characteristics of TA1 pure titanium under high strain rates and large strain ranges. Additionally, they modified the original model and combined it with a finite element analysis approach to establish a failure model based on stress triaxiality. Li et al. [29] investigated the mechanical properties of Q390D steel using the C-S model for the precise prediction of dynamic strength, while also enhancing this model to forecast the mechanical behavior at high strain rates reliably. Zhang et al. [30] proposed an improved multi-head attention module for predicting the mechanical properties of cold-rolled steel.

In summary, previous studies primarily investigated the static properties of Q460 steel; however, there have been limited studies on its dynamic properties. In this study, a combination of experimental and numerical simulations was used to perform static and dynamic tensile tests using an electronic servo-testing machine and SHPB. The J-C and C-S models were fitted based on the experimental results and numerical simulations were performed to evaluate the accuracy of the fits. Additionally, a numerical simulation of blast resistance was conducted based on fluid-structure interactions. The constitutive model developed in this study accurately describes the strain rate effect of Q460 steel. A numerical simulation of blast resistance was used to analyze the absorption of blast energy by steel plate structures under blast impact loading.

II. Test program

A. Materials

A 10 mm thick Q460 steel plate with a density of 7850 kg/m^3 produced by Qinhuangdao Shouqin Metal Material Limited was used in this study. Table 1 details its constituent elements.Figure 1 details the quasistatic specimen's dimensions. The original size satisfied the requirements of the composite tensile testing method at ambient temperatures [31]. In the SHPB tests, cylindrical specimens with dimensions of Φ10 mm×6 mm were utilized, as specified by reference [32].

B. Quasi-static tensile tests

An electro-hydraulic servo universal testing machine was employed to conduct quasi-static tension tests on all the specimens at room temperature with an experimentally loaded strain rate of 4×10^{-4}s^{-1}. Six specimens were used, and the tests were repeated on two specimens in each group.

TABLE I
CHEMICAL COMPOSITION OF THE Q460 STEEL (WT %)

C	Si	Mn	P	S
0.14	0.32	1.44	0.014	0.003

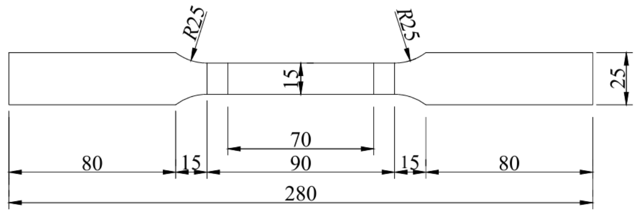

Fig. 1. Dimensions of the tensile specimen.

C. SHPB

The SHPB method is now the leading approach for analyzing materials' dynamic mechanical behavior at high strain rates [33]. Figure 2 shows a diagram of the SHPB testing apparatus. The complete system comprised a gas cabin, strike bar, incident bar, transmission bar, and an energy-absorption setup. The fundamental principle of SHPB tests involves the impact of a bullet on an incident bar under the influence of inflated pressure. This impact generates an incident wave (ε_I) within the bar, which transmits elastic stress waves onto the specimen. Because of the stress waves, the specimens underwent high-speed deformation. The specimen was relatively short when compared to the elastic bar. Consequently, when the stress waves rapidly pass through the specimen, reflected wave (ε_R) and transmitted waves (ε_T) are generated. The ε_R enters the incident bar, whereas ε_T enters the transmission bar.[34] In the testing apparatus, the striker bar measures 200 mm in length. Both the incident and transmission bars are considerably longer, clocking in at 1000 mm apiece. The compression bar, fashioned from high-strength manganese steel, has a diameter, φ, of 12.7 mm. Strain gauges were positioned on the central sections of the impact and transmission bars, and an oscilloscope recorded the respective pulse signals as they traversed the gauges. The classical two-wave method [35] was utilized during this process, in which the reflected and ε_T waves were monitored via the strain gauges, and the time-dependent relationship between stress, strain, and strain rate can be obtained using Equation 1.

$$\begin{cases} \sigma(t) = \dfrac{EA_0}{A}\varepsilon_t(t) \\ \varepsilon(t) = -\dfrac{2C_0}{l}\displaystyle\int_0^t \varepsilon_r(t)dt \\ \dot{\varepsilon}(t) = -\dfrac{2C_0}{l}\varepsilon_r(t) \end{cases} \quad (1)$$

where E and A_0 denote the Young's modulus and cross-sectional area of the elastic compression bar, respectively, C_0 denotes the speed of the strain wave for the elastic compression bar, and A and l denote the cross-sectional area and length of the specimen, respectively.

This research employed inflation pressures of 0.5, 0.6, and 0.8 MPa. Varying bullet pressures altered impact velocities, and the specimens experienced different strain rates when subjected to impact. Two sets of repetitive impact tests were performed for each inflation pressure to improve the test accuracy.

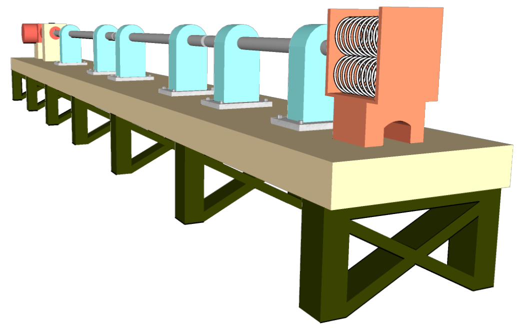

(a) Apparatus

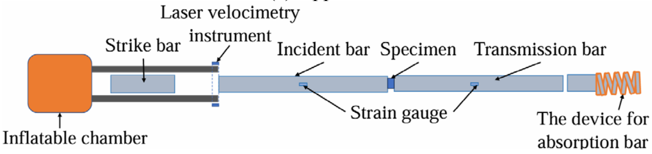

(b) Details

Fig. 2. SHPB testing system.

III. Results and Discussion

A. Experimental results

The tensile properties of Q460 are obtained based on three sets of quasi-static tensile tests, as listed in Table 2, and the average value of the test yield strength is used to obtain the yield strength of the specimen at 504 MPa. Figure 3's stress-strain curve shows Q460 attains its elastic phase yield strength of 512 MPa, subsequently transitioning into the yielding phase. As the strain increased, the stress exhibited jagged fluctuations before reaching the lower limit of yield. The steel then enters the hardening region, and the stress continues to increase with increasing strain. Q460 reached the tensile limit when the stress increased to 629 MPa, after which the specimen exhibited a necking phenomenon and the stress value decreased until fracture. Utilizing the average value of the three sets of tests, it was determined that the Q460 exhibited an elongation rate of 24.3%, which is close to the fracture strain value shown in Figure 3. Zhang [36] obtained an elongation of 24.5% for Q235 steel, which was close to that of Q460 steel. This suggests that the plasticity of the Q460 steel does not significantly decrease with increasing strength, indicating superior plasticity.

During the dynamic compression experiments, stress waveforms were recorded using an ultra-dynamic strain gauge and oscilloscope. Figure 4 illustrates the varying strain rate-induced dynamic compression waveforms for Q460 steel.

Figure 5 shows Q460's stress-strain behavior across strain rates of 546s-¹ to 1083s-¹. Steel has no significant yield region under dynamic loading, the dynamic yield stress corresponds to the stress associated with a 0.2% plastic strain [37]. The impact velocities generated by the bullets at different inflation pressures, associated strain rates, and the dynamic yield strength data of the specimens are listed in Table 3.

TABLE II

EXPERIMENTAL DATA FOR Q460 STEEL TENSILE TESTING AT ROOM TEMPERATURE

Specimen number	Thickness (mm)	Poisson's ratio	Yield strength (MPa)	Young's modulus E (GPa)	Elongation (%)
A1	9.7	0.3	511	228.5	24.3
A2	9.7	0.3	497	211.7	22.9
A3	9.7	0.3	504	219.8	23.4

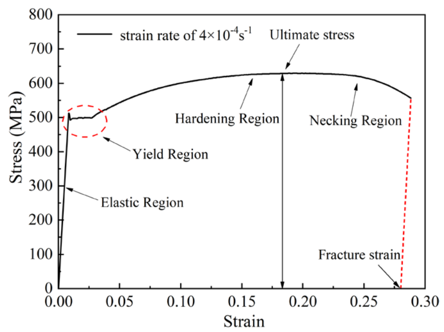

Fig. 3. Stress-strain curve of Specimen A3 at ambient temperature.

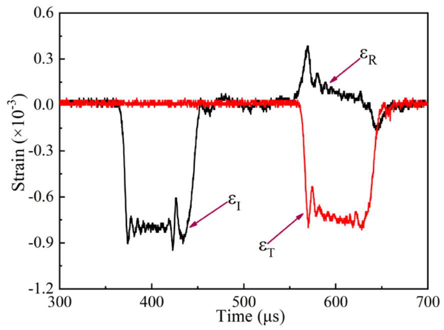

(a) 549 s^{-1}

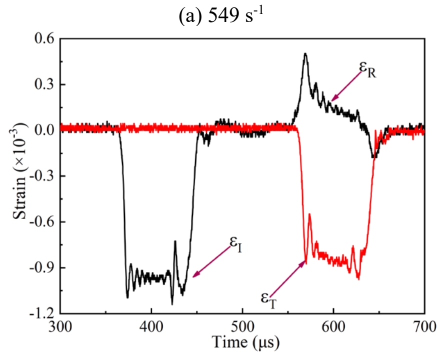

(b) 819 s^{-1}

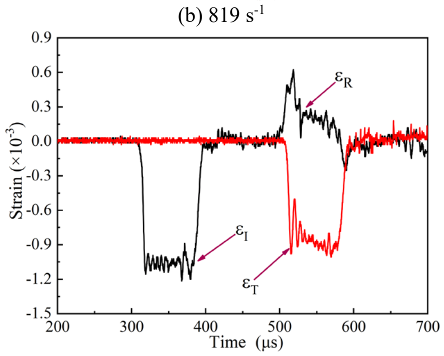

(c) 1083s^{-1}

Fig. 4. Stress waves in Q460 steel under different strain rates.

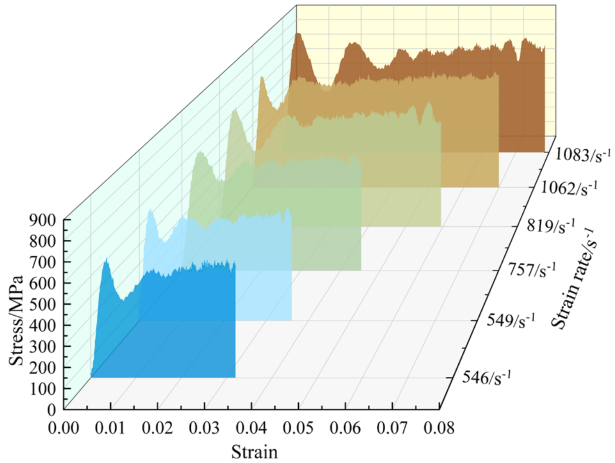

Fig. 5. Stress-strain curves of Q460 at different strain rates.

TABLE III
DYNAMIC COMPRESSION TEST DATA FOR Q460 STEEL AT AMBIENT TEMPERATURE

Experiment number	Inflation pressure/MPa	Impact velocity(m/s)	Strain rate/s^{-1}	Dynamic yield strength/MPa
A1	0.5	21.9	546	554
A2	0.5	21.9	549	556
A3	0.6	24.4	757	640
A4	0.6	24.4	819	664
A5	0.8	28.3	1062	701
A6	0.8	28.3	1083	714

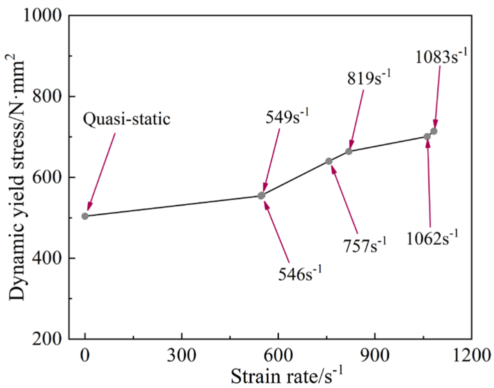

Fig. 6. Dynamic yield stress-strain rate curve of Q460.

Zhang [36] measured the yield strength and dynamic mechanical properties of Q235B and Q345B steels at quasistatic strain rates using SHPB experiments. In this study, the yield strengths of three steels were compared at similar strain rates. As listed in Table 4, the percentage increase in the yield strength of the Q460 steel was 41%, which was lower than those of Q235B and Q345B. By analyzing the yield strength growth rates of Q235B and Q345B at comparable strain levels, increased steel tensile strength correlates with diminished yield strength gains, and the strain rate's influence on yield strength diminishes.

TABLE IV
DYNAMIC YIELD STRENGTHS OF DIFFERENT STEELS

Steel type	Strain rate/s^{-1}	Dynamic yield strength/MPa	Quasi-static yield strength/MPa	Percentage increase in yield strength/%
Q235B	1437	540.2	265	90.3
Q345B	1233	571.8	360	58.8
Q460	1083	714	504	41

B. Dynamic increase factor (DIF) of yield stress

Figure 6 demonstrates the notable strain rate influence on Q460 steel, increasing from 4×10^{-4} s^{-1} to 1083 s^{-1}, the strength increases significantly, and the yield strength rises from 504 MPa to 714 MPa. The Dynamic Increase Factor (*DIF*) of yield stress has been established to quantify the extent of the strain rate effect on yield stress. The factor is based on the dynamic-to-quasi-static yield stress ratio.

TABLE V
DIF OF Q460 STEEL AT DIFFERENT STRAIN RATES

$\dot{\varepsilon}$ /s^{-1}	f_y/MPa	*DIF*
4×10^{-4}	504	—
546	554	1.099
549	556	1.103
757	640	1.270
819	664	1.317
1062	701	1.391
1083	714	1.417

C. C-S models

The C-S model utilizes a simple expression to depict the relationship between the *DIF* and strain rate, which can be formulated as:

$$I=\frac{\sigma_{\mathrm{dyn}}}{\sigma_{\mathrm{st}}}=1+\left(\frac{\dot{\varepsilon}}{D}\right)^{\frac{1}{p}} \tag{2}$$

where I denotes the *DIF* of Q460 steel, σ_{dyn} denotes the dynamic flow stress, σ_{st} denotes the quasi-static stress, $\dot{\varepsilon}$ denotes the current plastic strain rate, and D and P denote material parameters that require fitting.

The fitting parameters D and P can be obtained by considering the logarithms of both sides of Equation (2):

$$\ln\left(\frac{\sigma_{\mathrm{dyn}}}{\sigma_{\mathrm{st}}}-1\right)=\frac{1}{P}\left(\ln\frac{\dot{\varepsilon}}{D}\right) \tag{3}$$

Considering terms $\ln\left(\frac{\sigma_{\mathrm{dyn}}}{\sigma_{\mathrm{st}}}-1\right)$ and $\ln\varepsilon$ in Equation (3) for Q460 steel, Table 5 values enable material parameter fitting using the C-S model, which yields $D = 21300$ and $P = 3.7$.

The equation for the C-S model of the Q460 steel is shown in Equation (4):

$$\frac{\sigma_{\mathrm{dyn}}}{\sigma_{\mathrm{st}}}=1+\left(\frac{\dot{\varepsilon}}{21300}\right)^{0.27} \tag{4}$$

D. DIF of Q460

By performing a least-squares fitting of the experimental data provided in Table 5, the *DIF* of Q460 was determined.

$$DIF=1.057\dot{\varepsilon}^{0.03}\left(\dot{\varepsilon}\geq10\right) \tag{5}$$

The C-S model was established by fitting the *DIF*.

$$DIF=\frac{\sigma_{\mathrm{dyd}}}{\sigma_{\mathrm{s}}}=1+\left(\frac{\dot{\varepsilon}}{D}\right)^{1/P} \tag{6}$$

The *DIF* of Q460 steel can be expressed as follows:

$$DIF=1+\left(\frac{\dot{\varepsilon}}{21300}\right)^{0.27} \tag{7}$$

Yang's proposed prediction formula is as follows:

$$\frac{f_{y,d}}{f_y} = DIF_y = 1 + (\frac{\dot{\varepsilon}}{D_y})^{\frac{1}{P_y}} \tag{8}$$

$$D_y = 1000\left(\frac{f_y}{235}\right)^{3.8} \tag{9}$$

$$P_y = 5\left(\frac{f_y}{235}\right)^{-0.5} \tag{10}$$

By substituting f_y = 504 into Equation (8) and (9), the *DIF* of Q460 steel can be determined as follows:

$$DIF = 1 + \left(\frac{\dot{\varepsilon}}{18000}\right)^{0.29} \tag{11}$$

where $f_{y,d}$ denotes the dynamic yield strength, DIF_y denotes the *DIF* of the yield stress, and D_y and P_y denote the fitted yield stress parameters.

Figure 7 illustrates the correlation between *DIF* and strain rate for Q460 steel, which is verified using the dynamic constitutive model proposed by Yang. The fitted curve of the C-S model obtained in this study was close to the *DIF* curve of steel predicted by Yang, which established the validity of the C-S model.

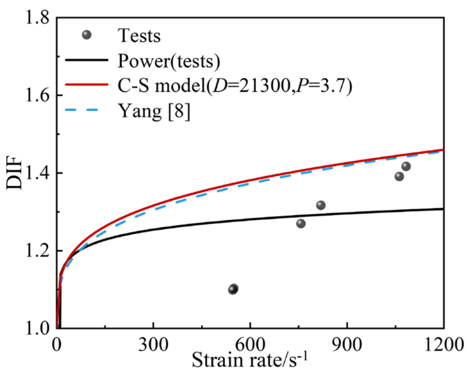

Fig. 7. Comparison of experimental data for different models (C-S model).

E. J-C models

The J-C material model establishes a functional relationship between the flow stress and various factors, including the equivalent plastic strain, relative equivalent plastic strain rate, and dimensionless temperature [38].

The general form of the J-C constitutive model can be expressed as:

$$\sigma = \left(A + B \times \varepsilon^n\right)\left[1 + C\ln\left(\dot{\varepsilon}/\varepsilon_0\right)\right]\left[1 - \left(\frac{T - T_r}{T_m - T_r}\right)^h\right] \tag{12}$$

where σ is the flow stress, ε is the equivalent plastic strain, $\dot{\varepsilon}$ is the reference strain rate, T_m, T_r and T are the material melting point, reference temperature and current deformation temperature (ºC), respectively A is the yield strength of the material under quasi-static conditions, B and n are strain-hardening parameters, C is the strain-rate sensitivity coefficient, and m is the thermal softening coefficient.

The J-C model considers three material effects: strain hardening, strain-rate hardening, and temperature softening. The formulation of this model encompasses three integral sections: the first part illustrates the strain-hardening effect of the material after entering the plastic phase; the second part describes the increase in material strength owing to the increase in strain rate; and the third component highlights the softening effect of the material strength at high temperatures.

In this study, the thermal softening effect due to adiabatic temperature increase was not considered. Thus, room temperature was maintained throughout the investigation (T=T_r). The general form of the J-C model was simplified by fitting only the terms related to stress and strain rate strengthening, as follows:

$$\sigma = (A + B\varepsilon^n)[1 + C\ln(\dot{\varepsilon}/\dot{\varepsilon}_0)] \tag{13}$$

1) Fitting parameters A, B, and n

where A denotes the yield strength of Q460 at the reference strain rate at room temperature, which can be obtained directly from the quasi-static curve: A = 504 MPa.

The strain rate was selected as the reference strain rate and Equation (13) can be simplified as:

$$\sigma = A + B\varepsilon^n \tag{14}$$

Equation (14) illustrates the stress-strain relationship of the material for a given reference strain rate, and $B\varepsilon^n$ describes the strengthening phase of the stress-strain curve for quasi-static experiments. Taking the logarithms of both sides in Equation (14) yields:

$$\ln\left(\sigma - A\right) = \ln B + n\ln\varepsilon \tag{15}$$

Furthermore, substituting into Equation (15) yields:

$$y = x + n\ln\varepsilon \tag{16}$$

The least-squares method was used to fit the $\ln\left(\sigma - A\right)$, ε to obtain the values of x and n, which could then be substituted into the equation to determine the value of parameter B. Parameters B and n were determined to be B=322 MPa and $n = 0.445$.

2) Fitting parameter C

Considering the case of a strain rate of 1083 s^{-1} by selecting a specific point on the stress-strain curve of the steel material and incorporating the previously determined values of A, B, and n into Equation (13), C can be calculated. In this case, the value of C was determined as 0.012.

At room temperature, the expression for the J-C model for Q460 at a reference strain rate of $4\times10^{-4}s^{-1}$ is provided by the following Equation:

$$\sigma = \left(504 + 322\varepsilon^{0.445}\right)\left[1 + 0.012\ln\left(\dot{\varepsilon}/0.0004\right)\right] \tag{17}$$

3) Relevant parameters of the J-C model should be referenced at a strain rate of 1 s^{-1}

When numerical simulations are performed using LS-DYNA, the utilized parameters are those corresponding to the reference strain rate $\dot{\varepsilon}_0$ =$1s^{-1}$. Consequently, by recalibrating parameters A, B, C, and n using the aforementioned methodology, it is possible to derive the constitutive equation of a material for numerical simulation calculations.

$$\sigma = \left(551 + 352\varepsilon^{0.445}\right)\left(1 + 0.11\ln\varepsilon\right) \tag{18}$$

The J-C model parameters' accuracy was confirmed by testing their behavior at varying strain rates, notably at 1 s^{-1}. The J-C model represented by Equation (17) and Equation (18) was applied separately at reference strain rates of 1 s^{-1} and 4×10^{-4} s^{-1}. By simplifying these equations, it was observed that the resulting simplified equations were consistent for both cases.

$$\sigma = 579 + 370\varepsilon^{0.445} \tag{19}$$

After verification, the J-C model parameters exhibited high accuracy at a strain rate of 1 s^{-1}.

F. Comparison of models and experimental results

A reliability assessment was conducted for the parameters of the C-S and J-C models through comparative analysis. This compared the stress-strain curves from both fitted models to experimental data at matching strain rates, thereby evaluating the accuracy of the fitted curves.

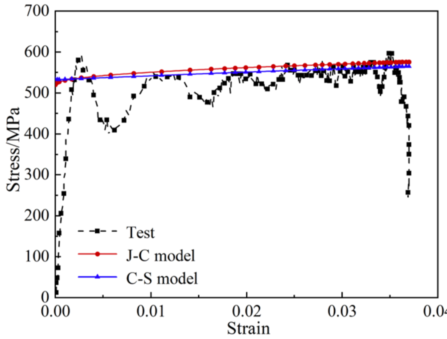

(a) 549 s^{-1}

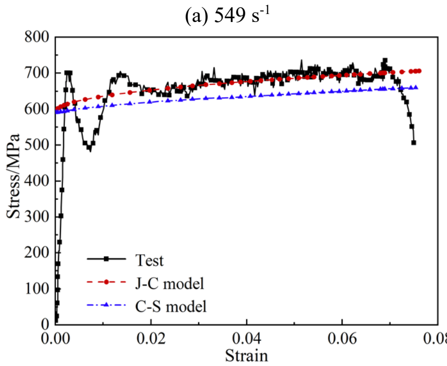

(b) 819 s^{-1}

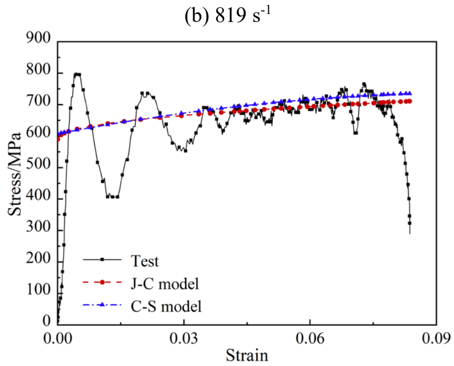

(c) 1083s^{-1}

Fig. 8. Comparison of test data obtained using models for different strain rates.

Figure 8 presents the J-C and C-S model fitting results across varying strain rates. A comparison of the fitted curves and experimental data revealed that at a strain rate of 549 s^{-1} (see Figure 8a), during the stage when slight oscillations of the stress occurred and tended towards stability, the fitted curves exhibited slightly higher stress values than those obtained experimentally. Notably, the C-S model exhibited a highly accurate fit. At a strain rate of 819 s^{-1} (see Figure 8b), there exists a significant disparity between the fitted curve generated by the C-S model and experimental results, indicating poor fitting accuracy. However, a remarkably accurate depiction of the stress variation with strain was achieved using the J-C model, which aligns closely with the experimental observations. Similarly, at a strain rate of 1083 s^{-1} (see Figure 8c), there was a marginal overestimation of the stress obtained using the C-S fitted curve compared with the experimental results. Conversely, the J-C model accurately represents the material behavior under dynamic conditions, as evidenced by its close agreement with the experimental findings. A comprehensive analysis suggests that for low strain rates, the C-S model effectively characterizes the dynamic constitutive relationships of materials, whereas for high strain rates, the J-C model better represents such relationships. Additionally, the J-C model's parameters showed greater reliability.

IV. Numerical simulation of SHPB

A. Finite element modeling

In the SHPB experiments, the experimental setup primarily comprised an inflation valve, a striker bar, an incident bar, a transmission bar, and an oscilloscope. Therefore, when establishing an SHPB experimental model using ANSYS software, it is essential to create finite element models of the four main components: the striker bar, incident bar, specimen, and transmission bar. Subsequently, the velocity functionality of the inflation valve is determined by setting the initial conditions of the striker bar. First, the finite-element software ANSYS was used to establish an SHPB experimental model. The diameters of the bars were set to 12.7 mm, the impact bar measured 0.2 m, incident and transmission bars, 1 m. Specimens were Φ10 mm × 6 mm in diameter. Given that the shapes of both the bar and specimen were cylindrical, to simplify the modeling process and reduce the solution time during the numerical simulation, a 1/4 model was built, and its boundaries were constrained.

In the finite element model, the solid element SOLID164 was employed for both the bars and specimens. The linear elastic state model was used as the input for bar material definition using the keyword *MAT_ELASTIC. The elastoplastic material model was used as the input for specimen material definition using the keyword *MAT_PLASTIC_ KINEMATIC. The first constitutive equation employed the C-S model with specific material parameters: $E = 210$ GPa, $\upsilon = 0.3$, $\rho = 7850$ kg/m^3, $D = 21300$ s^{-1}, $P = 3.7$. The second constitutive equation utilized the J-C constitutive model with specific material parameters: $A = 504$ MPa, $B = 322$ MPa, $n = 0.445$, $C = 0.012$, and a reference strain rate of $4\times10^{-4}s^{-1}$. The contact between the striker bar and the incident bar, as well as incident bar to specimen, and subsequently between the specimen to transmission bar contact type, is face-to-face contact type. The contact algorithm employed in this analysis is the default penalty function method available in LS-DYNA. The default value for the stiffness penalty factor within the contact parameters is set at 0.1, and it does not consider the frictional interactions between the contacting surfaces. In the process of calculating the solution time, according to the formula for solving the one-dimensional elastic stress wave velocity (E_0 is the modulus of elasticity of the bar, and is the density of the bar), it can be calculated that C_0=5172.2m/s. the lengths of both the incident and transmission bars are measured at 1000 mm, while the specimen has a length of 6 millimeters. The solution time is determined to be 0.0005s from the above data.

B. Comparison of numerical simulation and experimental results

Verification of J-C model and C-S model accuracies via SHPB numerical simulation. By extracting the strain-time curve from the unit located at the midpoint between the incident bar and transmitted bar, the variation in strain throughout the entire solution process for a given specimen was obtained, as illustrated in Figure 9.

The reflection and transmission of waves occurred simultaneously, as shown in Figure 9(a), thereby validating the correspondence between the strain and time waveforms fitted based on the numerical simulations and experimental measurements. To assess the precision of the modeled waveforms, a comparative study was executed, contrasting the simulated curves from varied models with the actual experimental waveforms. The J-C and C-S models exhibited satisfactory fit for the simulated and experimental waveforms of the incident wave, showing consistent waveform patterns during and before the oscillation phases. However, the simulated wave magnitude is marginally less than the observed data. The simulated reflection waveform closely matched the experimental results in terms of amplitude consistency, although some differences were observed when the rapid strain values decreased during the oscillation phase. The transmitted waveforms obtained from the numerical simulations exhibited a good fit with the experimental waveforms, albeit at smaller amplitudes. Nevertheless, it should be noted that there was a deviation in the peak values of the reflected waves compared to the experimental results for the C-S model. Specifically, the peaks in this model occurred earlier than those shown in Figure 9(b). In summary, while the three-wave waveforms generated by both the C-S and J-C models exhibited reduced amplitudes in comparison to the corresponding experimental curves. Notably, the waveforms generated by the J-C model alone closely corresponded to the experimental outcomes. This observation suggests a greater accuracy in the numerical simulations provided by the J-C model. In Figure 9(b), the oscillation amplitude of the three-wave waveform generated by the J-C model was marginally greater than that of the waveform obtained through experimental methods. In contrast, the C-S model yielded a three-wave waveform that exhibited a closer alignment with the experimental waveform, thereby demonstrating superior overall shape consistency. In Figure 9(c), the simulated C-S model's reflected wave amplitude demonstrates a reduced magnitude when compared to the amplitude yielded from experimental means. Conversely, J-C model simulations closely mirror empirical waveforms.

The C-S model yields a reliable fit between the numerical simulation and experimental waveforms at low-impact velocities. As the impact velocity increased, the J-C model outperformed the C-S model in fit. The results indicate that the proposed C-S model effectively simulates Q460 steel's low-speed mechanical behavior (low strain rates), whereas the J-C model is more appropriate for high strain rates. The fitted J-C model parameters are highly reliable, as they accurately capture a material's dynamic mechanical behavior under impact loading. The findings provide a foundation for studying constitutive relationships in additional steel types, which can reduce the cost associated with experimental characterization.

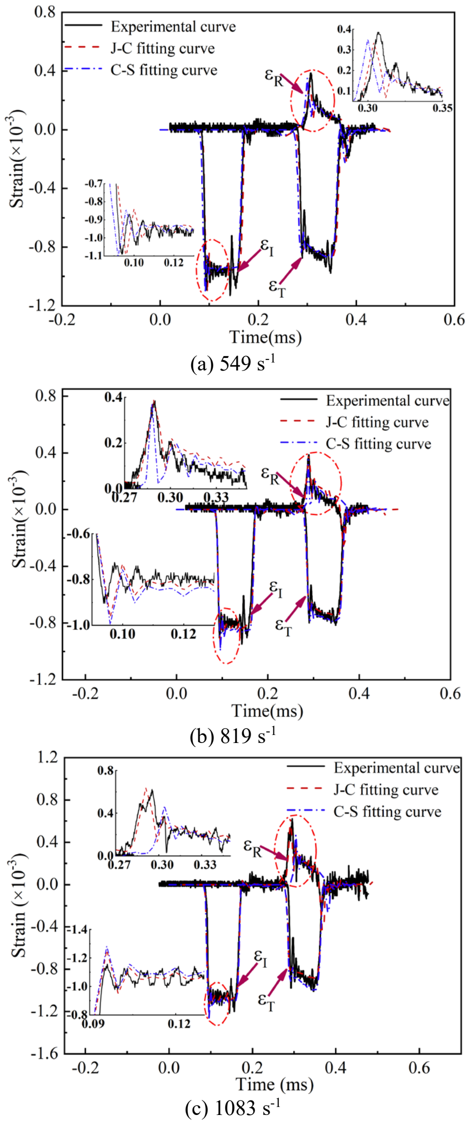

Fig. 9. Comparison of numerical simulation and experimental strain-time curves at different impact velocities.

C. Model accuracy analysis

To further assess the precision of the C-S, J-C, and experimental results in terms of their fitting accuracies, the wave fluctuation data for the incident, reflected, and transmitted waves were compared. The root mean square error (RMSE) [39] was employed to assess the overall precision of the J-C and C-S models in terms of fitting the experimental waveform.

$$RMSE = \sqrt{\frac{1}{N}\sum_{i=1}^{n}\left(Y_i - f\left(x_i\right)\right)^2} \tag{20}$$

where Y_i represents the experimental data, $f(x_i)$ represents the simulated data, and N represents the number of data points.

An analysis of the accuracy of the model is shown in Figure 10. J-C model calibration was contrasted with C-S model outcomes across varying speeds and waveforms. J-C model calibrations provided a superior fit compared to C-S. The findings confirm the J-C model accurately captures Q460's dynamic constitutive behavior.

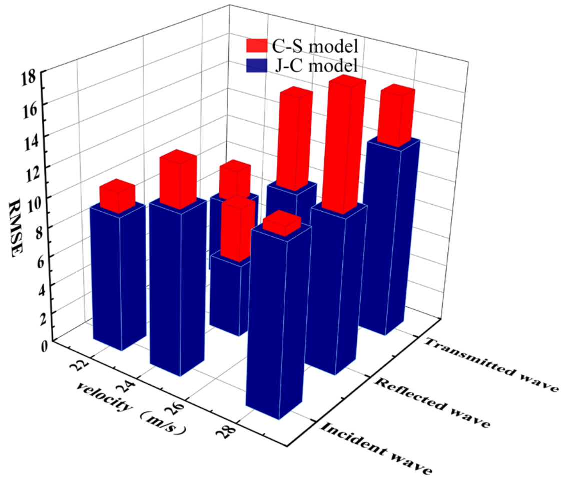

Fig. 10. Model accuracy analysis: Comparison of RMSE waveform values.

V. NUMERICAL SIMULATION OF IMPACT RESISTANCE

A. Finite element modeling

The model used in this section is a tunnel model in which the TNT is located at the entrance to the tunnel, and the explosion generates a shockwave of high pressure inside the tunnel. The object used in this study was a steel plate in a tunnel model, illustrated in Figure 11. The steel plate measured 1000 × 1000 × 10 mm, while the air domain measured 4200 mm × 1000 mm × 1000 mm. Additionally, the explosive utilized had a cubic configuration with side lengths of 80 mm × 80 mm × 80 mm, corresponding to a TNT equivalent of 0.83 kg. The front and rear faces of the air domain were reflection-free boundaries, and the remaining boundaries were defined as rigid walls.

The ANSYS software was used to model the steel plate, TNT, and air separately. Figure 11 illustrates the finite element model.

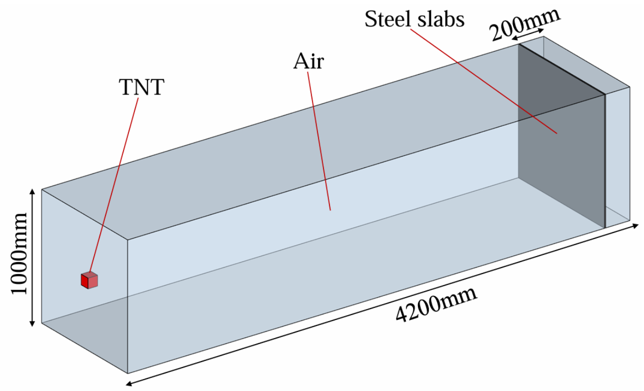

Fig. 11. Finite element model.

The steel plate was represented using the Shell163 element with a 20 mm mesh, while the TNT and air were modeled using the Solid164 element with a 40 mm mesh. The J-C model parameters were selected for the steel plate material and the parameter values were consistent with those of the steel used for the numerical simulation of the SHPB. MAT_NULL was used as the air material model. The fluid-structure interaction algorithm was used to simulate the shock response of an explosive shock wave. The model keyword for the TNT is *MAT_HIGH_EXPLOSIVE_BURN.

B. Analysis of numerical simulation results

Initially, a study of the steel plate's dynamic behavior under blast loading was conducted using center node 1401, and its displacement-time curve was analyzed, as shown in Figure 12(a). After 5 ms, the steel plate exhibited distinct displacement changes when the shock wave interacted with it, which caused the displacement to increase rapidly. The displacement had a maximum value of -0.026 m after 7.4 ms. Subsequently, the displacement direction of the steel plate changed was opposite to the direction of the shock wave pressure. The steel plate's displacement diminished as shock wave pressure exerted negative work on it. At 12 ms, the displacement of the steel plate in the opposite direction reached a maximum value of 0.016 m, and the same displacement change process occurred between 12 and 20 ms. From the displacement change curve of the node on the steel plate, the steel plate remained in the elastic deformation phase throughout the blast impact.

The center element 1226 of the steel plate was selected, and from Figure 12(a), it is evident that the steel plate yields at 8 ms, undergoes plastic deformation. At 18 milliseconds, the plastic strain recorded is 1.1%, with the corresponding displacement measured at 10 millimeters. Within 10 ms, the element accumulates a large amount of plastic strain at a high strain rate. Subsequently, the plastic strain changed gradually. The stress value of the element reached a maximum of 8 ms, and the maximum effective stress was 602 MPa. Subsequently, owing to the interaction of the shock wave with the surrounding rigid wall and steel plate structure during the propagation process, reflection superposition occurred, which led to a gradual decrease in stress. From Figure 12(a), it is observed that the element accumulates a large amount of plastic strain near 8 ms. Figure 12 (b) shows that the equivalent force at which the element starts to deform plastically is 631 MPa, which is 1.25 times the static yield strength owing to the strain rate effect considered in the material model. When the plastic strain reached 1.1%, the area enclosed by the stress-strain curve and the transverse axis accounted for a large portion of the total area. Furthermore, the energy absorbed by the material during a brief interval under impact loading represented the predominant portion of the total energy absorption.

The total energy curve of the steel plate during the blast impact is shown in Figure 13. Explosive shockwaves reached the steel plate after 5 ms, and the shockwave pressure interacted with the plate. The energy is then rapidly absorbed by the steel plate, and superposition occurs. At 7.7 ms, the total energy absorbed by the steel plate reaches a maximum of 4017 J. After the blast shockwave began to move away from the steel plate, the displacement and pressure directions were in contrast to the steel plate's total energy absorption, and the energy quantity decreased. The final direction of the displacement of the steel plate changed, and the direction of the shockwave pressure was consistent with the total energy curve. However, because the blast shockwave was far from the plate, the energy increase was very small. At approximately 15 ms, the total energy value tended to stabilize, the steel plate was no longer subject to the action of the shockwave, and the energy value was stable at 3119 J.

Moreover, the total energy value was associated with the entire process of the explosion impact of the steel plate.

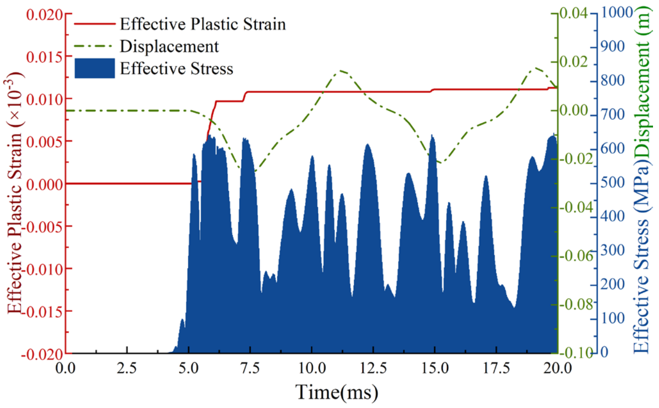

(a) Displacement–time, equivalent plastic strain-time curve, and equivalent stress-time curves of central element

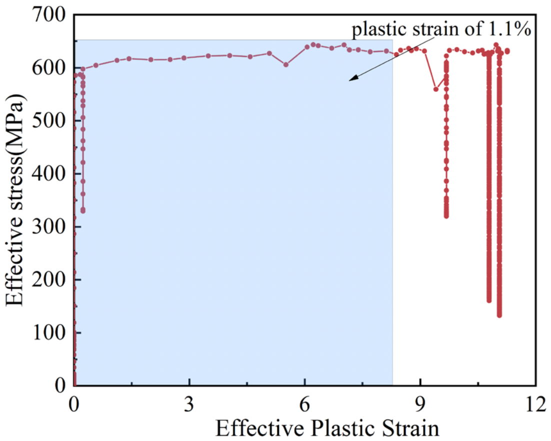

(b) Equivalent stress-equivalent plastic strain curve

Fig.12. Dynamic response of nodes and cells at the center of Q460 steel.

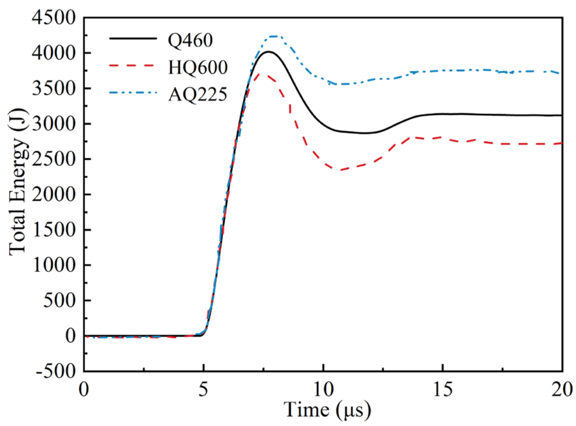

Fig.13. Total energy curves of different steels.

Numerical simulations revealed that the total energy absorbed by Q460 steel was 3119 J. The total energies absorbed by Q345 and HQ600 under the same conditions were 3156 J and 2895 J, respectively [40]. Furthermore, the strength of Q460 steel was found to be intermediate when compared to the strengths of these two materials. The energy intake of Q460 steel was marginally less than AQ255, yet more than HQ600 steel. It was determined that as the strength continued to increase, the ability of the steel to absorb the energy of the blast impact decreased.

VI. CONCLUSIONS

Quasistatic tensile tests were conducted using an electronic servo-testing machine. The tests were performed using the SHPB. The mechanical properties of the Q460 steel were investigated within a strain rate range of $1\times10^{-4}s^{-1}$-$1083s^{-1}$. The accuracy of the models was evaluated using SHPB tests in ANSYS. An air domain and the use of fluid-solid coupling analysis to simulate the mechanical properties of Q460 steel under the action of an explosive impact load and the absorption of energy were established. The main conclusions are as follows.

1) Q460 steel demonstrated strain rate sensitivity, as evidenced by an increase in its dynamic yield strength from 554 to 714 MPa when the strain rate was increased to 1083 s^{-1}.

2) The parameters of the C-S model were fitted according to the experimental data, D = 21300 and P = 3.7, and compared to those of the C-S model obtained by previous researchers in the field. It was determined that the C-S model used in this investigation was more accurate in predicting *DIF*. The parameters of the J-C model were determined using the least squares method to fit the data at a reference strain rate of $4\times10^{-4}s^{-1}$, A = 504 MPa, B = 322 MPa, n = 0.445, and C = 0.012.

3) A comparison and analysis of the stress-strain curves were performed based on the experimental data and the stress-strain curves fitted using the J-C and C-S models. The former effectively represents the dynamic constitutive relationship of Q460 steel at high strain rates, whereas the latter is suitable for fitting at low strain rates. An analysis of model accuracy utilizing the RMSE indicated that the J-C model demonstrated superior fitting results in comparison to the C-S model.

4) The finite element software ANSYS/LS-DYNA was employed to develop a pit model that incorporates explosives, steel plate specimens, and air domains. This model utilizes fluid-solid coupling analysis to investigate its capacity to absorb blast energy. A comparative analysis of energy absorption capabilities among Q345, Q460, and HQ600 steels indicates that Q460 steel exhibits a marginally lower capacity for absorbing explosive impact energy compared to Q345 steel. Conversely, HQ600 steel, which possesses higher strength, demonstrates a slightly superior energy absorption capacity relative to Q460 steel. This analysis suggests a trend wherein the capacity to absorb the blast energy of steel decreases as its strength increases.

REFERENCES

[1] Zheng KF, Zhang Y, Heng JL, Wang YW, "High strength weathering steel and its application and prospect in bridge engineering," Journal of Harbin Institute of Technology, Vol. 52, no. 3, pp1-10, 2020.

[2] Ju HT, Jiang W, Yang L, Yang JF, and Li BQ, "Research on the Application of High Strength Steel for 750 kV Combined Framework," IOP Conf. Series: Materials Science and Engineering, vol. 392, no. 2, pp022007, 2018.

[3] Zhao JJ, Guan YZ, Xue WQ, "Hot Roll Forming Analysis of Tapered Member of QP980 Steel for Lightweight Vehicles," Engineering Letters, vol. 28, no. 4, 2020.

[4] Zhu YL, Gao MZ, "Provincial Carbon Quota Allocation of China's Iron and Steel Industry Considering Environmental Factors Under the Goal of Carbon Peak," IAENG International Journal of Applied Mathematics, vol. 54, no. 3, pp465-474, 2024.

[5] GB 50017-2017. Standards for the design of steel structures. Beijing: China Architecture and Building Press, 2018.
[6] Fincato R and Tsutsumi S "Evaluation of the ductile fracture of Q460 steel under two different failure criteria," Procedia Structural Integrity, vol. 9, pp9126-135, 2018.
[7] Wang WY, Zhou HY, Xu L, "Creep buckling of high strength Q460 steel columns at elevated temperatures," Journal of Constructional Steel Research, vol. 157, pp414-425, 2019.
[8] Liao FF, Li XH, Wang W, Chen YY, Zhou TH, Nie SF, et al., "Seismic performance study on Q460 high-strength steel welded cruciform beam-column connections," Journal of Constructional Steel Res, vol. 198, pp107504, 2022.
[9] Zhao JY, Li J, Sun Y, "Experimental and numerical study on overall buckling behavior of Q460 high-strength steel continuous beams with welded singly symmetric I-section," Engineering Structures. vol. 280, pp115678, 2023.
[10] Yang XQ, Yang H, Gardner L, Wang YY, "A continuous dynamic constitutive model for normal- and high-strength structural steels," Journal of Constructional Steel Res, vol. 192, pp107254, 2022.
[11] Abhimanyu U, Jagadisha HM, Pratheeksha, "Numerical Investigation on the Performance of Concrete-Filled Double-Skin Tube Columns Under Blast Loading," Engineering Letters, vol. 32, no. 7, pp1394-1401, 2024.
[12] Ufuah E, Tashok TH, "Behaviour of Stiffened Steel Plates Subjected to Accidental Loadings," Engineering Letters, vol. 21, no. 2, pp95-100, 2013.
[13] Guo RQ, Ren HQ, Zhang L, Long ZL, Wu XY, Xu XY et al., "Research Progress of Large-diameter Split Hopkinson Bar Experimental Technique," Acta Armamentarii., Vol. 40, no. 7, pp1518-1536, 2019.
[14] Zhu XT, Zhang XJ, Yao WJ, Li WB, "Split-Hopkinson Pressure Bar Test of Silicone Rubber: Considering Effects of Strain Rate and Temperature," Polymers, vol. 14, no. 18, pp3892, 2022.
[15] Lena L, Tomáš F, Petr M, Manfred C, "Dynamic beam-end tests: Investigation using split Hopkinson bar," Int Journal Impact Eng, vol. 172, pp104417, 2023.
[16] Dong G, "The Numerical Simulation of Split Hopkinson Pressure Bar Experimental Technique," Dissertation, Hefei University of Technology, 2005.
[17] Ji JP, "Determination of the Thermo-Viscoplastic Constitutive Relations of 45# Steel," Transactions of Beijing Institute of Technology, vol. 28, no. 06, pp471-474, 2008.
[18] Zhang XH, Duan ZD, Li YS, et al., "Tests and numerical simulation for gas blast shock loading," Journal of Vibration and Shock, vol. 34, no. 10, pp142-146, 2015.
[19] Forni D, Chiaia B, Cadoni E, "Strain rate behaviour in tension of S355 steel: Base for progressive collapse analysis," Engineering Structures. vol. 119, pp164-173, 2016.
[20] Acharya S, Gupta RK, Ghosh J, Bysakh S, Ghosh KS, Mondal DK, and Mukhopadhyay AK, "High strain rate dynamic compressive behaviour of Al6061-T6 alloys," Materials Characterization, vol. 127, pp185-197, 2017.
[21] Chen JL, Shu WY, Li JW, "Constitutive model of Q345 steel at different intermediate strain rates," International Journal of Steel Structures," vol. 17, no. 1, pp127-137, 2017.
[22] Chen JL, Li JW, Li ZX, "Experiment research on rate-dependent constitutive model of Q420 steel," Construction and Building Materials. Vol. 153, pp816-823, 2017.
[23] Yang H, Yang XQ, Varma AH, Zhu Y, "Strain rate effect and constitutive models for Q550 high-strength structural steel," Journal of Materials Engineering and Performance, vol. 28, no. 11, pp6626-6637, 2019.
[24] Yang XQ, Zhu Y, Yang H, Zhang SM, "Investigations on CFST against lateral impact loading by FEA when employing rate-dependent models for different steel grades," Journal of Building Engineering, vol. 40, no. S1, pp370-377, 2019.
[25] Yang XQ, Yang H, Zhang SM, "Rate-dependent constitutive models of S690 high-strength structural steel," Construction and Building Materials, vol. 198, pp597-607, 2018.
[26] Mei YX, Ban HY, "High strain rate behaviour of stainless-clad bimetallic steel," Engineering Structures, vol. 207, pp110219, 2020.
[27] Jing L, Su XY, Feng C, Zhou L, "Strain-rate-dependent tensile behavior of railway wheel/rail steels with equivalent fatigue damage: Experiment and constitutive modeling," Engineering Fracture Mechanics, vol. 275, pp108839, 2022.
[28] Huang YF, Dong FX, Wu ZL, Cao QL, Chen Q, and Han XT, "Research on J-C constitutive and failure models for TA1 pure titanium sheet under high strain rate," Forging and Stamping Technology, vol. 48, no.03, pp236-243, 2023.
[29] Li H, Li FH, Zhang R, Zhi XD, "High strain rate experiments and constitutive model for Q390D steel," Journal of Constructional Steel Res, vol. 206, pp107933, 2023.
[30] Zhang QW, Guo RP, "Prediction of Mechanical Properties of Cold Rolled Steel Using Fusion of Multi-Head Attention," IAENG International Journal of Computer Science, vol. 51, no. 01, pp45-54, 2024.
[31] GB/T 32498-2016. Metal matrix composites, tensile testing—Method of test at ambient temperature. Beijing: China Standards Press,2017.
[32] Sun SF, Wu XT, Li HP, Meng YP, "Numerical simulation of effects of specimen size and shape in SHPB experiment," Journal of Hefei University of Technology(Natural Science), vol. 31, no. 09, pp1509-1512, 2008.
[33] Chen W, Lu F, Zhou B, "A quartz crystal-embedded split Hopkinson bar for soft materials," Experimental Mechanics, vol. 40, pp1-6, 2000.
[34] Wang LL, Wang YG, "The important role of stress waves in the study on dynamic constitutive behavior of materials by SHPB," Explosion and Shock Waves, vol. 25, pp1,2005.
[35] Song L, Hu SS, "Two-wave and three-wave method in SHPB data processing," Explosion and Shock Waves, vol. 25, no. 04, pp368-373,2005.
[36] Zhang XH, "Experimental research and numerical simulation on blast resistance performance of steel frames Dissertation," Harbin Institute of Technology,2011.
[37] Li JQ, Ma SZ, Mechanics of Explosion. Science Press, pp. 48-57,1992.
[38] Fan YF, Duan ZP, "Cylinder explosive test and material model of Johnson-Cook," Mech. Eng, vol. 25, pp40-43, 2003.
[39] Sun Q, Zhang ZL, Wu YB, Xu Y, Liang H et al., "Numerical Analysis of Transient Pressure Damping in Viscoelastic Pipes at Different Water Temperatures," Materials, vol. 15, no. 14, pp4904, 2022.
[40] Sun T, "Study of low yield point steel's dynamic constitutive relationship and its performance on explosion energy absorption," Harbin: Harbin Institute of Technology, pp41-58,2011.